

1 **First Detection of the Pekeris Internal Global Atmospheric Resonance:**
2 **Evidence from the 2022 Tonga Eruption and from Global Reanalysis Data**

3
4 Shingo Watanabe,^a Kevin Hamilton,^b Takatoshi Sakazaki,^c and Masuo Nakano^a.

5 ^a *Japan Agency for Marine-Earth Science and Technology (JAMSTEC), Yokohama, Kanagawa, Japan*

6 ^b *Department of Atmospheric Sciences and International Pacific Research Center, University of Hawai`i*
7 *Manoa, Honolulu, Hawai`i*

8 ^c *Graduate School of Science, Kyoto University, Kyoto, Kyoto, Japan*

9
10 *Corresponding author: Shingo Watanabe, wnabe@jamstec.go.jp*
11

ABSTRACT

We used observations and model simulation to examine the atmospheric pulses that dominate the far field in the hours after the January 2022 Tonga eruption. We analyzed radiance observations taken from the Himawari-8 geostationary satellite and showed that both a Lamb wave front with the expected horizontal phase speed $\sim 315 \text{ m-s}^{-1}$ and a distinct front with phase speed $\sim 245 \text{ m-s}^{-1}$ can be detected. The slower phase speed is consistent with that expected for the global internal resonant mode that had been proposed by Pekeris in 1937 and in other idealized theoretical studies over the past century, but which had never been detected in the atmosphere. A simulation of the eruption aftermath was performed with a high resolution atmospheric general circulation model. A hot anomaly over the volcano location was introduced instantaneously to the model fields and the model was integrated for another 12 hours. This produced a simulated wave pulse that, in the far field, agreed reasonably well with barograph observations of the Lamb wave. The model results also showed the presence of the slower pulse and that this disturbance had a vertical structure with a 180° phase shift in the stratosphere, in agreement with the theoretical prediction for the internal mode. An implication of this result is that the continuously ringing Lamb wave global normal modes that have been seen in analysis of long observational records ought to have lower frequency internal Pekeris mode counterparts, a prediction that we confirm through analysis of 57 years of hourly global reanalysis data.

SIGNIFICANCE STATEMENT

Our demonstration that both a surface-trapped Lamb wave and a slower horizontal phase speed internal Pekeris wave can be realized as normal modes of the global atmosphere resolves a very long-standing and fundamental issue in dynamical meteorology. Our result also has broader implications. The 2022 Tonga eruption produced a surprisingly large ocean tsunami even in a remote ocean basin, and it is possible that the slower atmospheric Pekeris mode can play a role in exciting the remarkable ocean response. Also the spectral peaks seen in atmospheric variability corresponding to the Pekeris normal mode provide features for comparison with global model simulations of the atmosphere, along with the Lamb modes detected in earlier studies.

1. Introduction

A fundamental and long-standing question in dynamical meteorology is whether and how the global atmosphere resonates. Unlike many familiar finite mechanical systems (such as a violin string, a drum membrane or an elastic sphere) that feature a complete set of possible normal mode oscillations, the unbounded nature of the atmosphere introduces complications and the expectation that the normal modes may not be a complete set. A true normal mode oscillation of the atmosphere must be described by solutions of the inviscid governing equations with no vertical energy flux at “infinite height”. It turns out that dealing with this subtlety has sustained a two century-long search for theoretical understanding and observational evidence of atmospheric resonance, as we will outline below. This brief historical Introduction both provides some context for this classic problem and serves as a useful introduction to the physical and mathematical issues that are involved. After this Introduction, we will show in this paper that observations following the explosive eruption of the Hunga Tonga–Hunga Ha'apai volcano on January 15, 2022, along with detailed computer simulations with a state-of-the-art global atmospheric model, as well as spectra of long records of atmospheric observations, allow a major advance in this long-standing issue, notably confirming for the first time the existence of the elusive internal vertical mode that has been a feature of theoretical solutions obtained by investigators in studies over the last 9 decades.

At the end of the 19th century Laplace (see Bowditch, 1829) laid the foundation for investigation of the global oscillations of the atmosphere, by formulating the mathematical theory for what we will call the “classical” problem. Specifically Laplace formulated the equivalent of the modern primitive equations on a rotating spherical earth for the small amplitude motions about a motionless mean state characterized by a mean temperature, $T_o(z)$, that is a function only of geometric height, z . Laplace showed that under these assumptions the solutions are separable in time, latitude, longitude and height. Further the equations governing the horizontal motions were identical to the Laplace Tidal Equations (LTE) that govern the motion of a barotropic ocean of some constant mean depth. For the free wave problem, the appropriate depth (today called the “equivalent depth”, h) needs to be found as an eigenvalue of a second order vertical structure equation. Laplace went one step further and derived a solution for the special case of an isothermal mean state and showed

that this had apparently only one eigensolution, and that solution had pressure perturbations exponentially trapped in the vertical (what we now call the Lamb wave).

The First Law of Thermodynamics had not yet been discovered, so Laplace's formulation and his results for h and the trapping depth of his Lamb wave solution are quantitatively incorrect (e.g. Finn, 1964). Later Lamb (1910) derived the correct analytic solution for the now familiar Lamb wave in an isothermal mean state. This is a hydrostatic, purely horizontally propagating, compressional wave with pressure perturbations and horizontal velocity perturbations varying as $e^{(\kappa-1)z/H}$ and $e^{\kappa z/H}$, respectively. Here H is the scale height for mean density, γ is the ratio of specific heats (~ 1.4), and $\kappa = (\gamma - 1)/\gamma$. The equivalent depth for this mode is $h = \gamma H$. With an assumed mean state temperature of 260K, $H \sim 7.6$ km and then $h \sim 10.7$ km.

Lord Kelvin (Thompson, 1882) suggested that the surprisingly large amplitude of the observed solar semidiurnal barometric oscillation, relative to both the solar diurnal and lunar semidiurnal oscillations, could be explained if the global atmosphere had a natural resonance that matched the semidiurnal frequency. This hypothesis ultimately turned out to be false, but it provided impetus for investigations over the following decades aimed at understanding the normal mode oscillations of the global atmosphere. Solutions to the LTE were refined by Hough (1897, 1898) and it was then possible to conclude that the solar semidiurnal resonance would require an equivalent depth close to 8 km (Chapman, 1924; Taylor, 1929).

Obtaining the equivalent depth by solving the vertical structure equation required a knowledge of the atmospheric temperature profile throughout the depth of the atmosphere and so was not a practical until well into the 20th century. Taylor (1929) sidestepped this issue and made a major contribution by noting that the pressure disturbance which had been observed in the far field after the 1883 Krakatoa eruption (Strachey, 1888) could be expected to propagate as a non-dispersive pulse at a horizontal phase speed of \sqrt{gh} (at least in the limit of a high-frequency short pulse for which the effects of planetary rotation can be ignored). The Krakatoa observations showed that the equivalent depth must be close to 10 km, and Taylor believed that this discredited the tidal resonance hypothesis. Similar results

were obtained later by researchers studying the pressure pulses observed after the 1907 Tunguska meteor event (Whipple, 1934) and after thermonuclear test explosions (Yamamoto, 1956).

The notion of a resonant semidiurnal tide was revived by Pekeris (1937) who made the first attack on quantitative solution of the vertical structure equation for a more general mean temperature profile. The tropopause had been discovered in 1902 and then, during the period from about 1920-1935, a series of investigations had revealed other basic features of the atmospheric temperature profile including the stratopause, mesosphere and mesopause (e.g., Hamilton, 2020). Pekeris solved the inviscid vertical structure equation for a mean state with layers corresponding to the troposphere, stratosphere and mesosphere with differing static stabilities. The upper boundary condition was enforced by specifying an isothermal mean temperature above the mesopause and demanding that solutions (e.g. for the pressure perturbation) in that region must decay exponentially. Pekeris found a solution similar to the idealized Lamb wave that was in phase in the vertical and had $h \sim 10$ km, but he also found that there was one other internal mode solution of the homogeneous problem characterized by a 180° phase shift near 30 km. Pekeris considered a mean temperature profile that had what we now know is an unrealistically high and warm stratopause, and for that case found that the internal mode had $h \sim 8$ km.

Jacchia and Kopal (1952) examined the normal modes by solving the vertical structure equation including an idealized forcing and plotting out the amplitude of the solution as a function of the equivalent depth assumed. They also considered a mean state with an unrealistically warm stratopause and in that case found resonant responses for both $h \sim 10$ km and $h \sim 8$ km.

Salby (1979) computed the homogeneous solutions to the inviscid vertical structure equation with realistic mean temperature profiles and found that there were two solutions, one corresponding to the $h \sim 10$ km external Lamb mode and one to the internal mode that Pekeris had revealed. However, with a realistic mean state Salby found that the internal mode has $h \sim 5.8$ km.

Salby (1980) investigated the forced solutions of the vertical structure equation, now adapted to include a reasonable representation of dissipative processes. He found a damped resonant response corresponding to the Lamb wave and also weaker responses, notably one that is evident particularly at stratospheric levels with $h \sim 6.4$ km and which seems to correspond to the internal mode revealed in solutions of the inviscid equation by Pekeris (1937) and Salby (1979).

Salby's results finally discredited the tidal resonance hypothesis, but by then the correct explanation for the strength of the solar semidiurnal tide had been found (Chapman and Lindzen, 1970). Somewhat earlier the relevance of the free Lamb wave solution in the day-to-day atmospheric circulation was confirmed when the westward-propagating "five day wave" was detected in observations and identified with the gravest wavenumber one Rossby mode solution for an atmosphere with $h \sim 10$ km (Madden and Julian, 1972; Hirota and Hirooka, 1984). Other prominent observed westward-propagating planetary waves were later also identified as global normal modes with the Lamb-wave vertical structure. Later Matsuno (1980), Hamilton (1984) and Hamilton and Garcia (1986) found peaks in spectra of observed hourly surface pressure that apparently correspond to zonal wavenumber 1 and 2 $h \sim 10$ km Kelvin modes (with the expected periods of about 33 and 16.5 hours, respectively). Recently Sakazaki and Hamilton (2020; hereafter SH2020) analyzed 38 years of hourly global reanalysis data and found space-time spectral peaks that clearly correspond to a large number of Rossby, Kelvin, Rossby-gravity and gravity modes of an $h \sim 10$ km atmosphere. (Details will be discussed later, but Fig. 9a below shows the spectrum of the tropical surface pressure resolved into eastward and westward propagating zonal Fourier wavenumbers and frequencies compared with the theoretical results for $h \sim 10$ km).

So we now see that the global atmosphere continuously rings at planetary scales at the expected wavelengths and frequencies for an $h \sim 10$ km atmosphere and for periods ranging from a few hours to a few days. Still unanswered is the question of whether the theoretically predicted internal mode can be manifest in the real atmosphere. Certainly the atmosphere is much more complicated than the simple theoretical models used in Salby (1979, 1980), notably in having mean states with horizontal winds and horizontal temperature gradients as

well as featuring an array of dissipative processes from surface friction to strong molecular diffusion in the thermosphere. Salby (1980) speculated that in the real atmosphere his internal mode solution was likely to be “of dubious significance”.

The idea of global resonance was invoked more recently by Forbes and Zhang (2012) to possibly explain the observed lunar tidal winds in the upper atmosphere. Specifically they suggested that the resonance between the lunar semidiurnal (L_2) tide (~ 12.42 hr period) and the internal mode may occur in a special case (they called this “Pekeris resonance”). They found that the L_2 tide was amplified in the upper air during a sudden stratospheric warming (SSW) event. Using a global linear wave model, they attributed the amplification to the resonance between L_2 and one of the internal, gravity modes which could only occur under somewhat special background temperature/wind distributions during SSWs.

The atmospheric response to the explosive eruption of the Hunga Tonga–Hunga Ha'apai volcano on January 15, 2022 was quite remarkable. Pressure pulses were seen at barograph stations throughout the world and the leading front of the pressure changes arrived at times consistent with the expected Lamb wave horizontal phase speed. Remarkably, the propagation of waves away from the eruption could be seen in satellite radiance observations (Duncombe, 2022; Adam, 2022). The satellite images reveal a complicated pattern of outward propagating waves in the vicinity of the eruption (many are likely vertically propagating waves) but the far-field is dominated by a wave front that corresponds to the Lamb wave mode seen as the initial pulse in the barograph data. Here we analyze geostationary satellite radiance observations in the hours after the eruption and show that in addition to the Lamb mode there is a wave front that corresponds to the slower phase speed expected for the internal normal mode. The identification of the internal mode is then confirmed by analysis of a new high resolution global atmospheric model simulation of the eruption aftermath. This result led us to slightly extend and reconsider the SH2020 investigation of the spectra of historical reanalysis data, and we will show that continuous ringing of global modes with the internal vertical structure is apparent in these data as well.

Note that we will refer below to the internal normal mode solution and its physically realized atmospheric effect as the “Pekeris wave” or “Pekeris mode” just as the more familiar surface-trapped solution is known as the “Lamb wave”. We want to advance this as a new standard nomenclature and Appendix A below presents a very brief discussion of some related history.

Section 2 below describes the satellite, ground based and reanalysis data sources we used, as well as a high resolution atmospheric general circulation model (AGCM) and the details of the Tonga eruption model integration. Section 3 discusses the results of our analysis of the observed data and AGCM simulation over the first hours after the Tonga eruption. Section 4 describes our extension of the SH2020 analysis of global reanalysis data, with a focus on the detection of the internal Pekeris mode. Conclusions and suggestions for further work are given in Section 5.

2. Data and Methodology

a. Himawari 8 data

We used the brightness temperature data at the 9.6μ band observed by Himawari 8, which is gridded at a ~ 4 km resolution and distributed by the Center for Environmental Remote Sensing (CEReS), Chiba University, Japan (Takenaka et al., 2020; Yamamoto et al., 2020; <ftp://hmwr829gr.cr.chiba-u.ac.jp/gridded/FD/V20190123/>). The signatures of the Lamb and Pekeris modes were apparent in different Himawari 8 emission bands, but were most clearly seen at 9.6μ . The Himawari 8 data is available every 10 minutes, and we calculated the 10 minute difference to extract the signal of rapidly propagating wave fronts that we anticipated for the Lamb and Pekeris wave modes.

b. Global model simulation data

We performed a global model simulation of the whole neutral atmosphere (0~150 km height) to see responses of the atmosphere to the explosive volcanic eruption. The Japanese Atmospheric General circulation model for Upper Atmosphere Research (JAGUAR,

Watanabe and Miyahara, 2009) was configured to have global triangular spectral truncation T2559 (~5 km horizontal resolution). This model includes a full set of physical parameterizations necessary to represent effects of sub-grid scale phenomena from the surface to the lower thermosphere. It has 340 vertical layers with a constant log-pressure height interval of 300 m throughout the middle atmosphere. An important point is that the top of this model is sufficiently elevated to avoid undesirable effects at the upper boundary that are generally present in typical global atmospheric models (e.g., Lindzen et al., 1968). In this high-resolution model, the parameterized Richardson number dependent turbulent diffusion induced by the wave breaking of explicitly resolved gravity waves is important as a momentum dissipation process near the mesopause, while the parameterized molecular viscosity, which strengthens exponentially with altitude, is important as a momentum dissipation process near the upper boundary, i.e., in the lower thermosphere. Those will provide appropriate constraints on the vertical structures for the Lamb and Pekeris modes. Note that JAGUAR is formulated using hydrostatic governing equations, a restriction that still allows the proper representation of the purely horizontally propagating compressional waves of the Lamb and Pekeris types, but which can distort other high frequency acoustic and gravity waves generated by the eruption.

The model was initialized by using spectral nudging in which components with total horizontal wavenumber 0-40 are nudged to the Modern-Era Retrospective analysis for Research and Applications version 2 (MERRA-2; GMAO, 2015). The nudging was performed for 12 hours from 16:30UT 14 January 2022 to obtain initial conditions at 04:30 UT 15 January 2022. Then a top-heavy thermal type of temperature disturbance extending over 850-400 hPa, diameter of 280 km and the magnitude of 100K near the center, was imposed over Hunga Tonga – Hunga Ha’apai. This timing was chosen because it corresponds to the time when the volcanic plume reached the stratosphere and its umbrella clouds expanded rapidly, as observed by the Himawari 8. We integrated for 12 hours with results saved every 5 minutes. Results for the sea level pressure were saved every 1 minute. The time step for the time integration was 1 second. The detailed simulation of the processes involved in the explosive eruption is not possible, but our simple approach of introducing a hot anomaly results in a simulation of the far field wave pulses that agree reasonably well with actual barometric observations in terms of the duration and amplitude of the pressure

perturbations. Thus, the simulation should be appropriate for the present purposes. In addition to the eruption simulation, a parallel non-perturbed control simulation was performed from the same initial conditions but without the added temperature disturbance. We found that, over our relatively brief integration period, the eruption minus control fields very effectively highlighted the wave perturbations due to the eruption.

This version of the JAGUAR model is computationally expensive as it is run with (i) very fine vertical resolution and deep domain in order to realistically treat the dissipation in the upper atmosphere and avoid unrealistic effects at the model top, and (ii) very fine horizontal resolution so that the relatively narrow wave fronts generated by the eruption can be well resolved. This expense has thus far limited the integration to just 12 hours post-eruption, but that could be extended in future investigations.

c. Barograph data

To evaluate the pressure pulse associated with the Lamb and Pekeris modes simulated by the GCM, we used surface pressure (P_s) data from a remarkable array of over 1500 barographs deployed throughout Japan in what is called the SORATENA weather sensors by Weathernews Inc. These measure surface air pressure at 1 minute intervals. We will also focus on one particular SORATENA station, at Jimbocho in Tokyo (35.696°N, 139.754°E). We will also use barograph observations at 6-minute resolution taken at a coastal buoy off Honolulu (21.303°N 157.865°W). The buoy is operated by the National Buoy Data Center of the U.S. National Oceanic and Atmospheric Administration.
(https://www.ndbc.noaa.gov/station_realtime.php?station=00uh1)

d. ERA5 data

Following SH2020, we will analyze hourly surface pressure time series with $1^\circ \times 1^\circ$ longitude-latitude grids from the latest reanalysis dataset produced by the European Centre for Medium-Range Weather Forecasts (ECMWF), ERA5 (Hersbach et al., 2020). While SH2020 analyzed data during 1979-2016, in the present study we additionally analyze data between 1950 and 1978 (Bell et al., 2021), so that a total of 57 years of data are processed.

The zonal wavenumber-frequency spectrum is calculated with the same methodology as in SH2020, and it is only briefly described here. In order to detect interhemispherically-symmetric and meridionally-coherent modes we analyze fields that were averaged at each longitude between 20°S and 20°N. Then a 2D zonal-time Fourier transform is applied. (SH2020 also considered antisymmetric modes, but in the present paper we will restrict our attention to the symmetric modes). The calculation is made for individual years (the first 365-day data are processed even for leap years) and the spectra are then averaged over the 57 years. To empirically determine the vertical structure of any identified modes, regression analysis is used (again, see SH2020 for details): First, we first produce an “index time series” by applying zonal wavenumber-frequency filtering to equatorially averaged surface pressure data. Then, a specific zonal wavenumber component of equatorially averaged ω on 37 pressure levels are regressed onto this index to obtain the vertical structure of amplitude and phase. The amplitude is rescaled by multiplying the regression coefficient a factor of $\sqrt{2}\sigma$, where σ is the standard deviation of the index. The phase is relative to the variation surface pressure at 0°E; the values between 0 and π (π and 2π) denote ω takes a maximum eastward (westward) of pressure maxima.. Note that we do not assume any *a priori* vertical structure or zonal propagation direction (i.e., eastward or westward) for this analysis.

3. Results for the Response to the Tonga Eruption

a. Propagation of wave fronts observed by Himawari 8

Figure 1 shows the 10-minute time difference of brightness temperature at 9.6 μm observed by Himawari 8 plotted about 4 hours after the eruption (difference of 08:40UT – 08:30UT, 15 January 2022). The positive and negative values pair of rings about 5,000 km away from the volcano and a somewhat smaller radius pair of rings with a similar structure are clearly visible. These must be wave fronts which were excited by the explosive volcanic eruption and then spread rapidly, reaching various parts of the Pacific coast in a few hours. The data reported from many barographs showed that the fastest wave front circled the earth several times (Adam, 2022; Duncombe, 2022) as had the pressure front observed after the 1883 Krakatoa eruption (Strachey 1888; Taylor, 1929).

08:40UT 15 January 2022

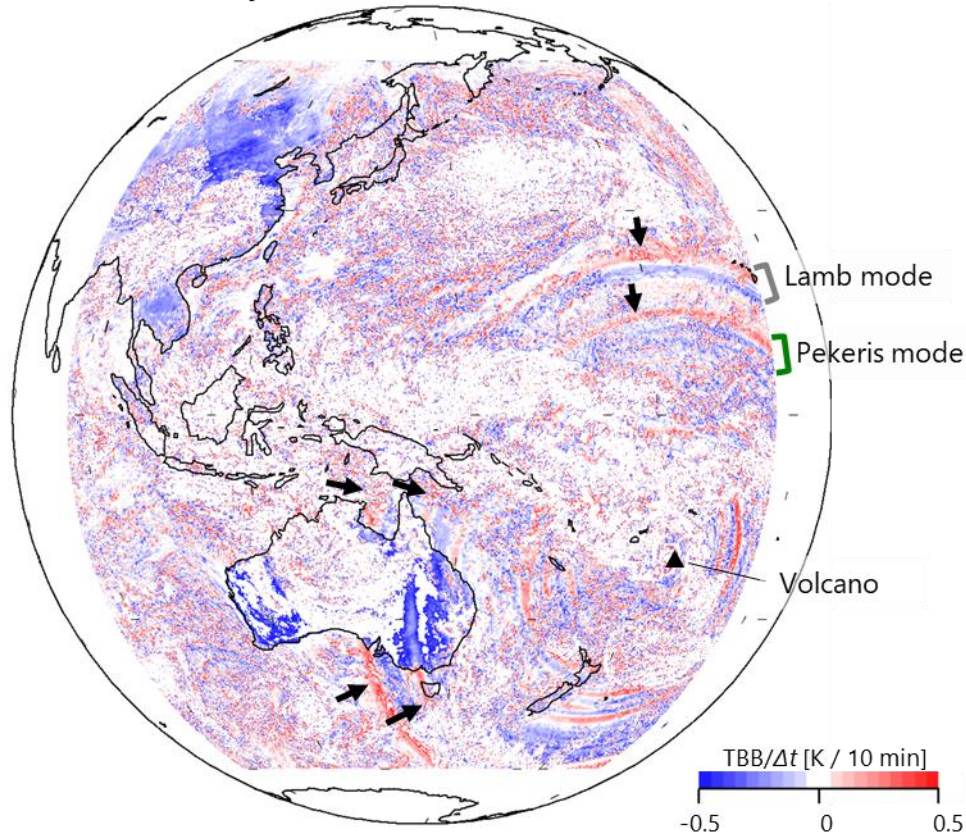


Fig. 1. The 10-minute difference of the 9.6 μm brightness temperature observed by Himawari 8 plotted about 4 hours after the eruption (difference of 08:40UT – 08:30UT, 15 January 2022). Our identification of the wave fronts associated with the Lamb and Pekeris modes are marked. The Gaussian filter was applied 10 times and shadings outside the minimum and maximum of the color scale are omitted for clarity.

Figure 2 shows the latitude-time cross section for the time difference in brightness temperature in the 9.6 μm band of Himawari 8 on the meridian passing over the volcano. There are clearly a number of pulse-like signals that can be seen propagating away from the latitude of the eruption. The first pulse to reach each location features a positive value for about 20 minutes followed by a negative value for about 10 minutes followed by another positive value. This wavefront can be followed to 60°N (which it reaches in ~7 hours) and to 60°S (~4 hours after eruption). This is compared in the figure to a subjectively determined constant phase velocity for each of the northward (315 m s^{-1}) and southward propagation directions (315 m s^{-1}). A distinct, slower moving, wave pulse is also identifiable propagating

across the whole 60°S-60°N region. This also has positive and negative values and stretches over ~40 minutes in the far field. In Fig. 2 this pulse is also compared with subjectively determined constant phase velocities (245 m s⁻¹ northward and 270 m s⁻¹ southward). Each of these two pulses hold together fairly well as they propagate, although they may show some small degree of dispersion. We identify these first two pulses reaching the far field with the Lamb and Pekeris mode theoretical solutions. Additional wave fronts propagating at a slower speed are also found around the volcano although these are not as clear in the far field, and likely represent gravity waves that have a vertical component in their propagation.

The phase velocities of the wavefronts are not perfectly isotropic because they are affected by the background temperature structure and wind, and so we estimated phase speeds for both modes by computing the distance of the wavefronts from the volcano three hours after the eruption and then averaging this distance with respect to the azimuthal angle around the volcano. This leads to values about 315 m s⁻¹ for the Lamb mode and 245 m s⁻¹ for the Pekeris mode.

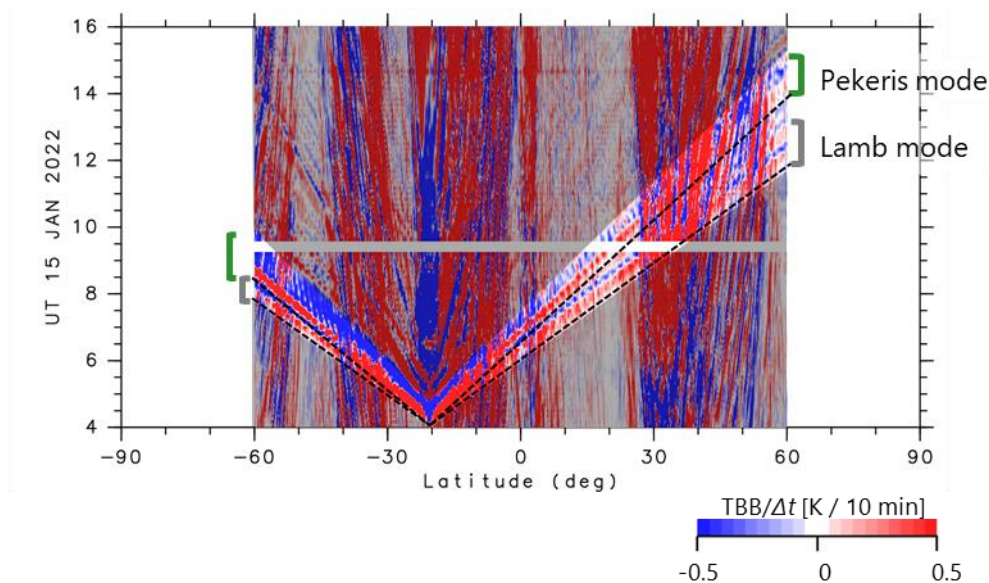


Fig. 2. Meridional propagation of the wave fronts of the Lamb and Pekeris modes as illustrated by a latitude-time cross section of the 10 minute time difference of the 9.6 μm brightness temperature observed by Himawari 8. Regions of particular interest are highlighted for clarity.

b. Propagation of pressure pulses simulated by JAGUAR GCM

Figure 3 shows the differences of SLP between the eruption and control simulations plotted at about 4 hours and 7 hours after the eruption, which correspond roughly to the times of arrival of the initial wave front at Honolulu and Tokyo, respectively. The Lamb wave front appears on the figure as two close spaced concentric circles with a band of high pressure (red) followed by low pressure (blue). The total width over two bands is very roughly 650-700 km. This Lamb wave front seems to propagate without much apparent dispersion over the 2.5 hours between the snapshots in Fig. 3. The horizontal outline of the wave front remains nearly circular but, even in these snapshots within several hours of the eruption, some modest deviation from a purely circular front is visible.

Inside the Lamb wave front in Fig. 3 is a slower moving circular front apparent as a transition from zero or positive pressures (red) to a well-defined band of falling pressure (blue). A band of high pressure (red) is apparent in the figure to the west, northwest and southwest of the volcano, but is not so clear to the east. As we will show, this front has horizontal phase speed and vertical structure consistent with that expected for the Pekeris normal mode and so it is labelled as such in Fig. 3. The horizontal outline of the wave front remains nearly circular but its center shifts westward with time, presumably due to the asymmetric background conditions.

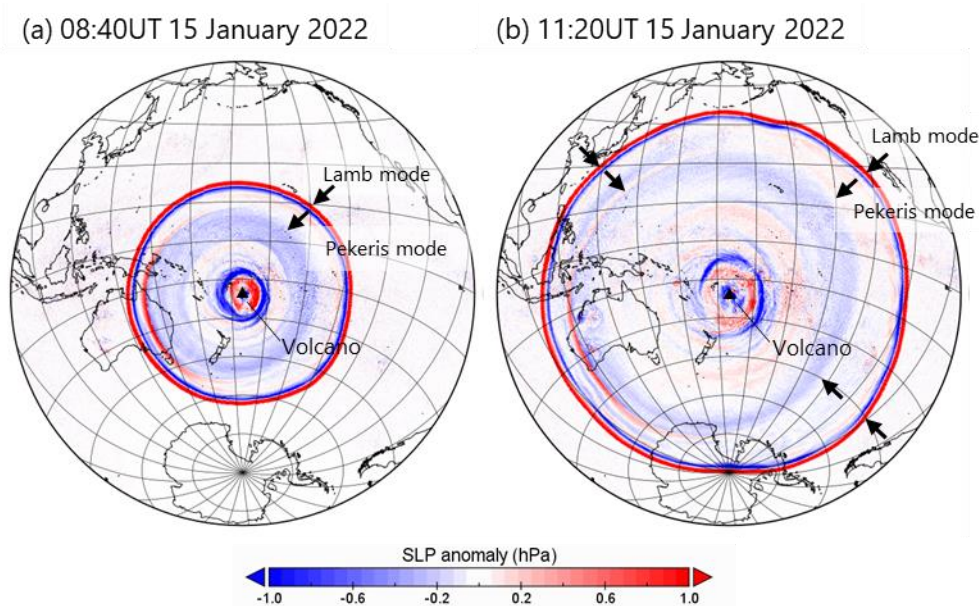


Fig. 3. The SLP difference between the eruption and control simulations of the GCM plotted at two different times several hours after the eruption. The arrows mark the wave fronts we identify with the Lamb and Pekeris modes.

Figure 4 shows the horizontal propagation of SLP disturbances in the GCM simulation in the same format as Fig. 2, but for propagation in the zonal direction. (The zonal direction is used here as the Pekeris mode signal in the GCM simulation is best defined west of the volcano). In Fig. 4 the Lamb wave front is apparent and commences with a high pressure (red) and then a low pressure (blue) and then another brief period of high pressure (red) with the pulse stretching over about 30 minutes. On the west side of the volcano the slower Pekeris mode front is apparent beginning with high (red) and then low (blue) pressures. On the east side of the volcano, the Pekeris mode front is apparent beginning with the low (blue) pressures. The propagation of each of the fronts displays a very constant phase speed. The dashed black lines in Fig. 4 approximately show the phase speeds of the Lamb and Pekeris modes averaged over the first 3 hours after the eruption and correspond to 323 m s^{-1} for the westward propagating Lamb mode front, 302 m s^{-1} for the eastward propagating Lamb mode front, 246 m s^{-1} for the westward propagating Pekeris mode, and 215 m s^{-1} for the eastward propagating Pekeris mode. These differences in the westward and eastward phase speeds are probably associated with the asymmetric background conditions, e.g., zonal flows and static stabilities, and will be validated against several barograph observations below.

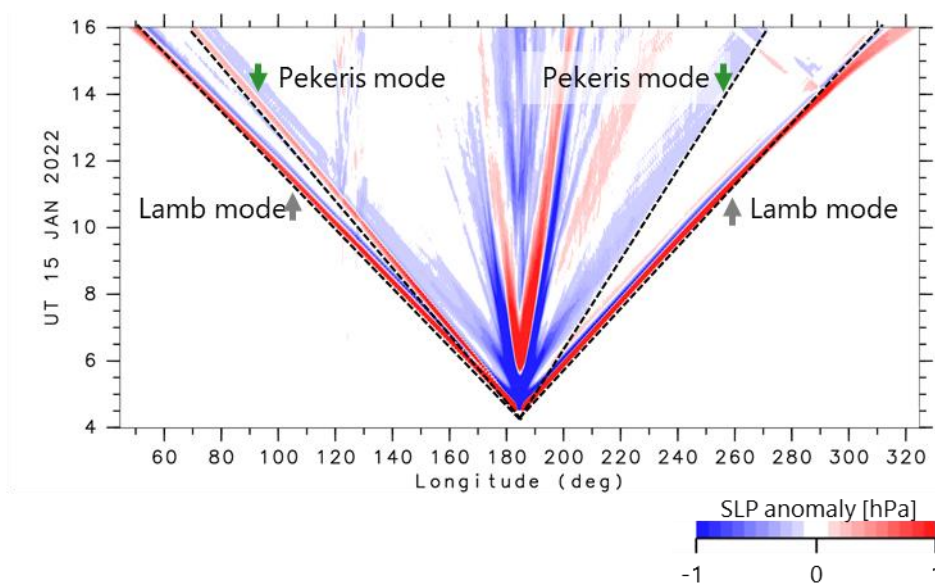


Fig. 4. Longitude-time cross section for the SLP difference between the eruption and control simulations of the GCM. Latitudinal average of 17.55-23.55°S was taken to reduce small scale fluctuations.

Figure 5 shows the time series of sea level pressure simulated by the model at three locations. Nuku'alofa (~140 km away from the volcano) is shown as an example of a point near the volcano, Honolulu (~5,390 km) as an example of a point northeast of the volcano, and Tokyo (~7,835 km) as an example of a more distant point northwest of the volcano. At Nuku'alofa, the pressure rises by about 20 hPa immediately after the eruption, then drops sharply by about 60 hPa peak-to-peak in about 10 minutes, and then returns to the pre-eruption pressure in about 20 minutes. At this close location we do not expect to be able to distinguish the separate Lamb and Pekeris modes. In Honolulu (Fig. 5b), the simulated pressure began to rise about four hours after the eruption, increased by about 3 hPa in about 10 minutes, then decreased by about 4 hPa from peak to peak over about 15 minutes, and then increased again. This series of increases and decreases in SLP is due to Lamb mode. The possible arrival time of a wave front with speed 247 m-s^{-1} is marked in Fig. 5b as well, and there may be a very slight corresponding pressure pulse in the simulated result. At Tokyo (Fig. 5c), which is located farther away from the volcano, the rising and falling pressure signals of the arrival of the Lamb mode front are similar to those seen at Honolulu, though with slightly lower amplitude. The positive pulse associated with the Lamb mode arrives in Tokyo about 6 hours and 40 minutes after the eruption. At Tokyo there may be a pressure pulse identified with the Pekeris mode commencing at about 8 hours and 50 minutes after the eruption (the time marked by the arrow which corresponds to a phase speed of 233 m-s^{-1}).

The observed pressures shown in Fig. 5 for Honolulu and Tokyo show fairly clearly the arrival of pulses at nearly the same time as in the simulation. The rise, fall, rise pattern is apparent in both station observations, although the observed pulse lasts for somewhat longer than the simulated pulse. At Tokyo the slower phase speed Pekeris mode pulse seems fairly clear in the simulation, but is less clear in the observations plotted for this single station.

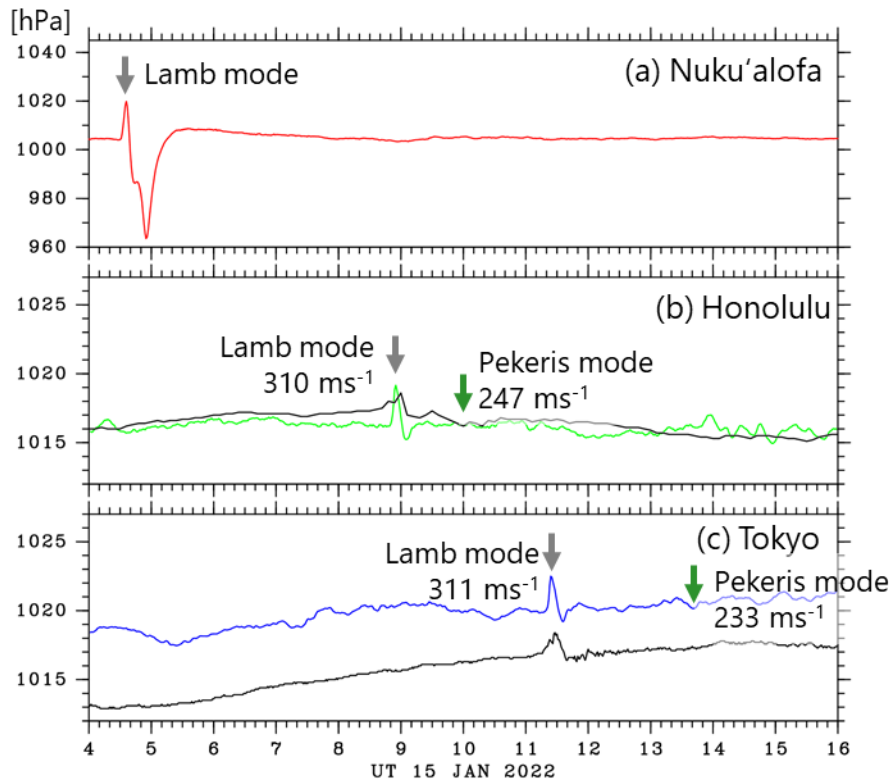


Fig. 5. Time series of sea level pressure in the hours after the eruption. Model simulated results are shown in the colored curves and the estimated arrival of the fronts associated with the Lamb and Pekeris modes are marked. For Honolulu and Tokyo the grey curves show observed barograph data.

c. Passage of pressure pulses over Japan

As noted in Section 2c above, the SORATENA array covers Japan with 1-minute barograph data at >1500 locations at this time. Figure 6 shows GCM simulated and SORATENA observed pressure tendencies over Japan at times corresponding to the arrival of the Lamb mode and the Pekeris mode. Figure 7 shows the individual (gray) or composited (colored) time series of surface pressure variations observed by SORATENA (panel b) and those of sea-level pressure reproduced by JAGUAR (the difference from the control run) at the nearby grids to the SORATENA stations (panel c). To extract the coherent variations, the data are sorted such that time “zero” corresponds to the timing of arrival of first pressure positive peak associated with the Lamb mode. The results are also categorized and analyzed separately based on the arrival time, or equivalently (assuming a constant phase speed), the distance from Hunga-Tonga (see panel (a)). The initial pressure rises and then falls and then

453 rises in the Lamb wave pulse; this is well defined in both the simulation and the observations
454 around 11:50 UT, although the width of wave front in the simulation is only about half that in
455 the observations.

456
457 The passage of the Pekeris mode almost two hours later also seems well defined both in
458 the observations and the simulation (Figs. 6c-f and 7). Again, the shape of the wave front is
459 somewhat different between the observations and the simulation. In the observations, the
460 wave front is characterized by a broad negative anomaly, while that in the simulation has a
461 marked positive anomaly preceding the sharp pressure fall. Note that the simulated wave
462 front arrives in Japan about 5 minutes after the observed front, indicating just a very slight
463 difference in horizontal wave phase speeds between the model and the real atmosphere.

464
465 Another feature is the increased “noise” in the SLP field following the initial passage of
466 the Lamb wave front (compare Fig. 6a with Fig. 6c, or see the variation in the time range of
467 10-100 min in Fig. 7). Notably, Fig. 7 shows that the different composite results have
468 coherent variations even for these “noisy” pattern, suggesting that these are the manifestation
469 of some systematic disturbances rather than any local noise. A similar variation after the
470 Lamb wave front passage is found in barograph observations at other locations around the
471 world. An example is a very high resolution barograph trace from Mauna Kea in Hawai`i
472 that has been published on the web by the US National Science Foundation
473 (<https://noirlab.edu/public/images/ann22003b/>). The increased disturbances could reflect the
474 development of instabilities set off by the passage of the Lamb pulse, but also could be from
475 other kinds of infrasound perturbations excited by the eruption (note that JAGUAR is a
476 hydrostatic model so that there are no acoustic waves with any vertical component of
477 propagation included). Our simulated results in Fig. 6a,c,e thus suggest that the response can
478 be divided into two wave fronts (Lamb and Pekeris) that have the expected form of circle arcs
479 that are concentric with the eruption far away, plus some enhanced small-scale disturbances.

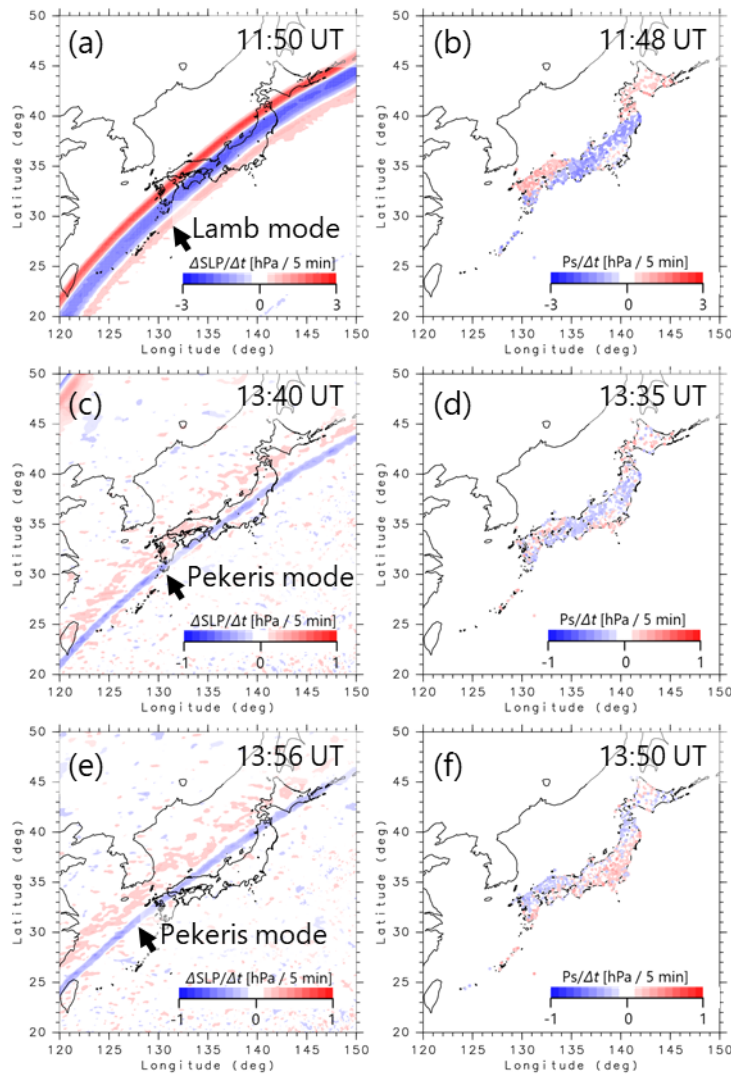


Fig. 6. The passage of the Lamb and Pekeris modes over Japan as identified by (a, c, e) the 5-minute time difference for the SLP difference between the eruption simulation minus control simulation of the GCM and (b, d, f) the 5-minute time difference of surface pressure observed by the SORATENA barograph stations.

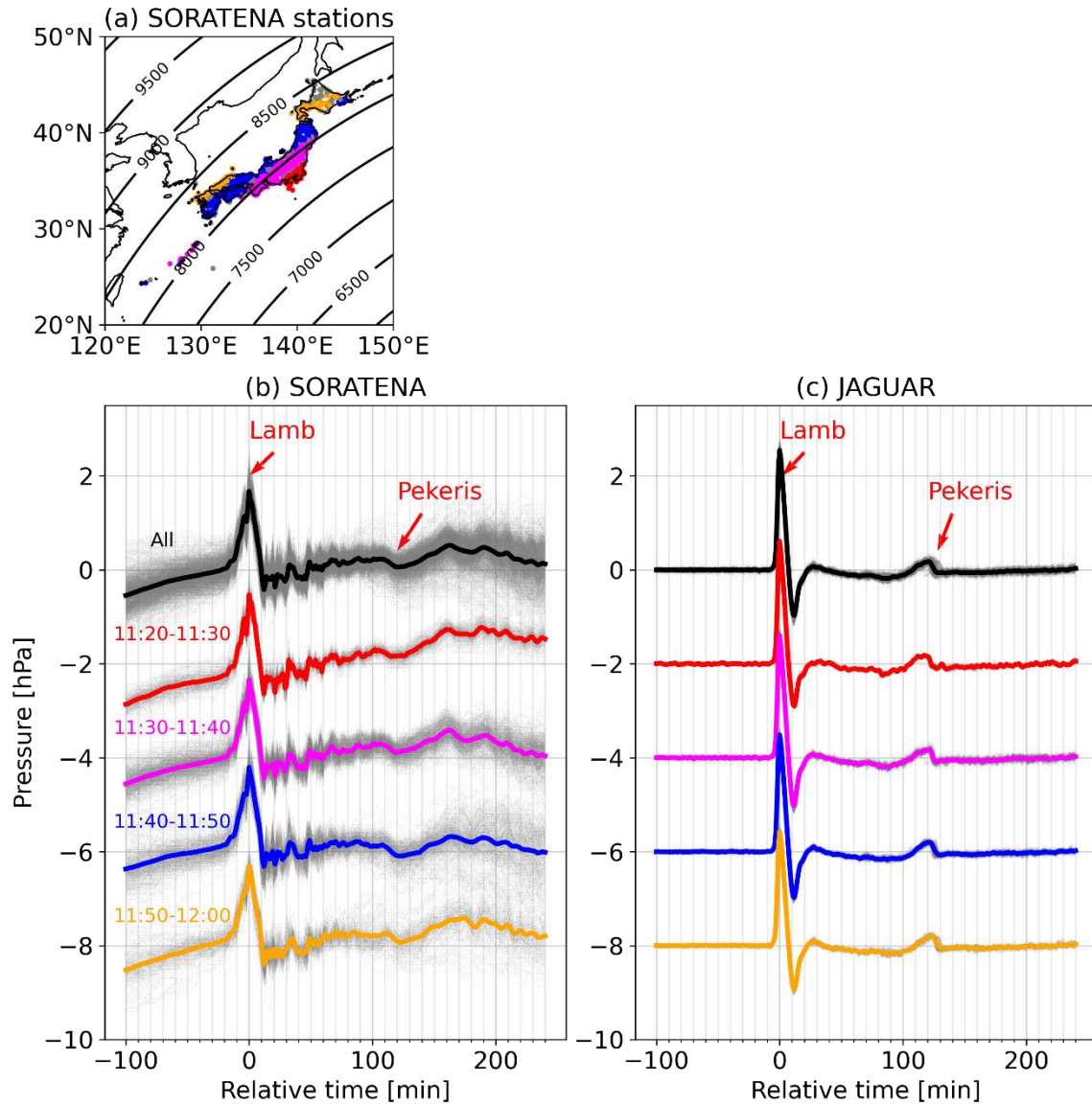


Fig. 7. (a) Distribution of SORATENA stations. Stations are categorized and colored depending on the arrival time of first wave front as defined as the local maximum of pressure variation during the analysis period (09:00-16:00UT, 15th, Jan). See panels (b) for color allocation (stations out of all of the categories are colored gray). Contours denote the great circle distance from Hunga Tonga (20.5°S, 175.4°E) (unit: km). (b)-(c) Time series of (b) SORATENA surface pressure data and (c) JAGUAR sea-level pressure data. For the JAGUAR results, the difference from the control run is analyzed. Anomalies from their time-mean at individual stations are plotted by thin gray curves, after being shifted such that the arrival time of wave front (defined as the maximum value during the period) occurred at time zero. Thick solid curves are the composite-mean for these anomalies. Plotting is categorized depending on the arrival time (panel (a)) and it is shifted arbitrarily 2 hPa for clearer presentation.

d. Vertical structure of atmospheric pulses simulated by the GCM

Figure 8 presents results from the model simulation designed to show the vertical structure of the wave fronts we have identified as the Lamb mode and Pekeris mode. Specifically shown in the figure are instantaneous vertical profiles at about 4 hours after the eruption for the vertical air pressure velocity, ω , scaled by $(P_s / p)^{5/7}$, where P_s and p are local surface pressure and atmospheric pressure, respectively. Results are averaged over several adjacent model grid columns located at the western extreme of the wave fronts. The scaling in the vertical we applied is based on the idealized inviscid Lamb wave solution for an isothermal mean state, and in that case would lead to a constant value throughout the atmosphere. In fact our result for the Lamb mode in Fig. 8 has a nearly constant magnitude throughout the troposphere and the stratosphere, while it has a modest peak in the mesosphere. By contrast the Pekeris mode profile has a node at about 90 hPa and has an amplitude which is stronger in the stratosphere and mesosphere than in the troposphere. These features basically agree with those found for the Pekeris mode in the theoretical solutions of Salby (1979, 1980).

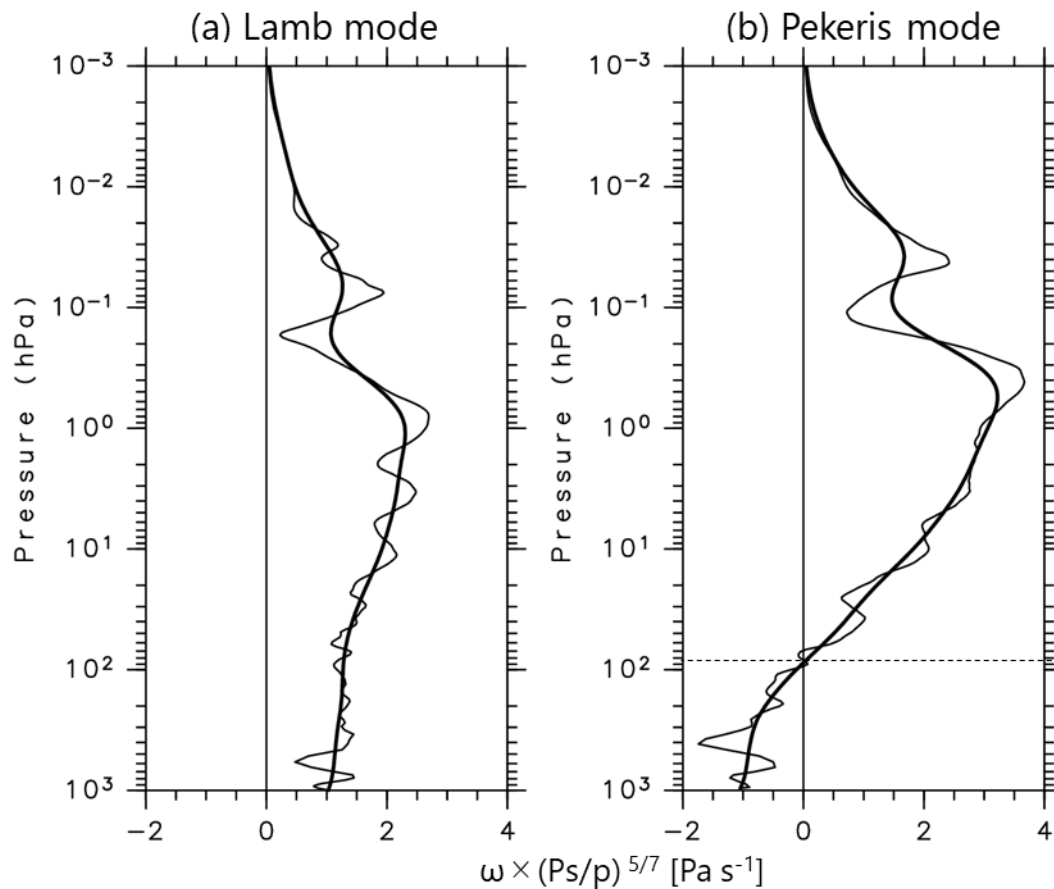


Fig. 8. Vertical structures of the Lamb and Pekeris modes simulated in the GCM. The vertical profiles of $\omega \times (P_s/p)^{5/7}$ [Pa s⁻¹] at 08:40 UT on 15 January 2022 at (a: 20S-21°S, 136.2°E) and (b: 20S-21°S, 144.7°E) are shown. Thin curves show original profiles, while thick curves show those smoothed by applying a 1-2-1 filter 300 times.

4. Results for Continuously Ringing Modes

Much of the atmospheric response to a sharp impulse, like that from a volcanic eruption, can be expected to take the form of vertically propagating waves that are eventually dissipated in the upper atmosphere. However, the initial perturbation will also project to some extent on the vertical normal modes of the atmosphere and that will lead to purely horizontally-propagating, nearly non-dispersive, wave pulses which will dominate the far field response. The ordinary processes in the atmosphere will also be expected to excite a continuous ringing of the global modes with the same normal mode vertical structures. This continuous ringing can be detected in Fourier spectral analysis of long data records.

The present study of the Tonga eruption aftermath demonstrates that the phase speeds of Lamb mode and Pekeris mode (in the limit of large wavenumber and frequency) are ~315 m s⁻¹ and ~245 m s⁻¹, respectively. Based on the relation, $c = \sqrt{gh}$, the corresponding equivalent depths are determined as 10.1 km and 6.1 km, respectively, purely based on these observations. This estimate of h of the Lamb mode is consistent with the previous estimates based on the speed of pressure pulse from Krakatau (Taylor, 1929) (10.4 km) and that based on the observed global normal mode frequencies by SH2020 (very close to 10 km; see also the present Fig. 9). By contrast, h of the Pekeris mode has been newly identified by the volcanic pulse observations in this study; this value is roughly consistent with theoretical expectation by Salby (1979,1980) (close to 6 km).

SH2020 analyzed 38 years (1979-2016) of hourly surface pressure and geopotential height data in ERA5 reanalyses and discovered evidence for a large number of Rossby, Rossby-gravity, Kelvin and gravity modes with Lamb wave properties. As part of the present project we have repeated the SH2020 analysis for the longer 1950-2016 ERA5

record. Figure 9a shows the zonal wavenumber-frequency power spectrum of the surface pressure averaged over 20°S-20°N compared with the theoretical predictions for the inter-hemispherically symmetric modes of an $h=10.1$ km atmosphere. The excellent agreement of observed and theoretical spectral peaks is evidence that the global atmosphere is ringing simultaneously at many possible resonant frequencies corresponding to the Lamb wave vertical structure.

We have outlined earlier our evidence from satellite data and GCM simulation for the existence of both an external Lamb wave and an internal Pekeris normal mode in the response to the impulsive forcing from the Tunga eruption. This leads us to reexamine the long record of global data in a search for the possible presence of continuously ringing global modes with the Pekeris mode vertical structure. Fig. 9b shows the surface pressure spectrum expanded to show just the lower frequency results. Fig. 9c repeats this but with the theoretically predicted frequencies for the modes with $h=10.1$ km (solid circles) and also for $h=6.1$ km (open circles) shown. The predictions for each horizontal mode are now pairs with the Pekeris mode having the lower frequency. For at least the wavenumber 1 and wavenumber 2 Kelvin waves there is a clear indication of a power maximum near the predicted Pekeris mode frequencies. Fig. 9d shows the power spectrum for the eastward propagating wavenumber 1 and 2 components. Results are shown for both the full record and for just the post-1978 period. For both the wave 1 and wave 2 spectra there are two peaks standing clearly above the background, one corresponding closely to the predicted result for $h=10.1$ km, and the other centered at a slightly higher frequency than that for the $h=6.1$ km prediction. The two distinct peaks are most clearly recognized for the small-wavenumber Kelvin modes and are not so visible for Rossby and gravity modes. For the high-frequency waves (Kelvin, gravity) these two frequencies are well separated so that they can be distinguished, while for the low-frequency Rossby modes the expected Lamb and Pekeris mode frequencies are quite close together (see Fig. 9c) and difficult to resolve in observations. For the higher frequency modes the amplitudes are found to drop off with increasing frequency and the meridionally gravest Kelvin modes have more energy than the gravity modes. So we expected that the Pekeris mode peaks would be most likely to be detectable for the wavenumber 1 and 2 Kelvin modes, and indeed this is clearly seen in our results (Fig. 9c). In Fig. 9c there may be some indication of Pekeris mode peaks for other

horizontal modes, notably for the westward propagating zonal wavenumber 1 gravest gravity mode, but we will not pursue this further in this paper.

Figures 10a and 10b show the vertical profiles of amplitude and phase, respectively, in vertical air pressure velocity, ω , correlated with the eastward wavenumber 1 variations with frequencies around the two peaks that were apparent in Fig. 9d. Note that we have scaled the amplitude in Fig. 10a by $(P_s / p)^{5/7}$, as we did for Fig. 8 earlier. See Section 2 above for more details on the method, and note that the horizontal red bars in Fig. 9d show the frequency range included in the filtering for each peak. It should be again noted that this data analysis does not assume any *a priori* structure for the vertical dependence. In agreement with SH2020, the Kelvin waves associated with the $h=10.1$ km peak indeed have a theoretically expected Lamb mode structure, with the amplitude growth close to $(p / P_s)^{5/7}$, and with almost no vertical phase progression. The waves associated with the $h=6.1$ km peak, by contrast, have the character of an internal Pekeris mode, as they show a node around 100 hPa (see the phase jump there) with their amplitude maximizing near the surface as well as in the upper stratosphere. This vertical structure agrees well with that of the Pekeris mode wave front as simulated by the JAGUAR GCM (Fig. 8) and with Salby's expectation that the energy is ducted near the surface as well as in the upper stratosphere.

SH2020 did not draw attention to the Kelvin wave peaks associated with the Pekeris mode ($h=6.1$ km), which - while definitely smaller than the Lamb mode peaks - are indeed apparent in SH2020's figures 6h and 7h. The present analysis of the atmospheric pulses caused by the Tonga eruption led us to conclude that the small peaks appearing in the 2D spectrum are meaningful, and we now identify them as the resonant internal mode oscillations of the sort identified in idealized theoretical studies by Pekeris (1937), Jacchia and Kopal (1952) and Salby (1979, 1980).

Inspection of our Fig. 9d reveals an unrelated, but possibly interesting, feature of the ERA5 spectrum. SH2020 analyzed all the hourly ERA5 data available to them (1979-2016), but since then ERA5 has been extended back to 1950. So our Fig. 9d compares the spectra computed over 1979-2016 and over 1950-2016. For the most part the two curves agree well,

and it is gratifying that the agreement is very good for the Lamb and Pekeris mode peaks we identified. However there is a systematic difference in the wavenumber 1 spectrum for periods shorter than about 20 hours, namely the power over 1979-2016 is noticeably weaker. So, over the period assimilating NOAA operational satellite radiances, the power at very large horizontal scales and high frequencies is smaller than over the earlier (largely pre-satellite) period. This may be an interesting issue for the procedures used in the ERA5 assimilation.

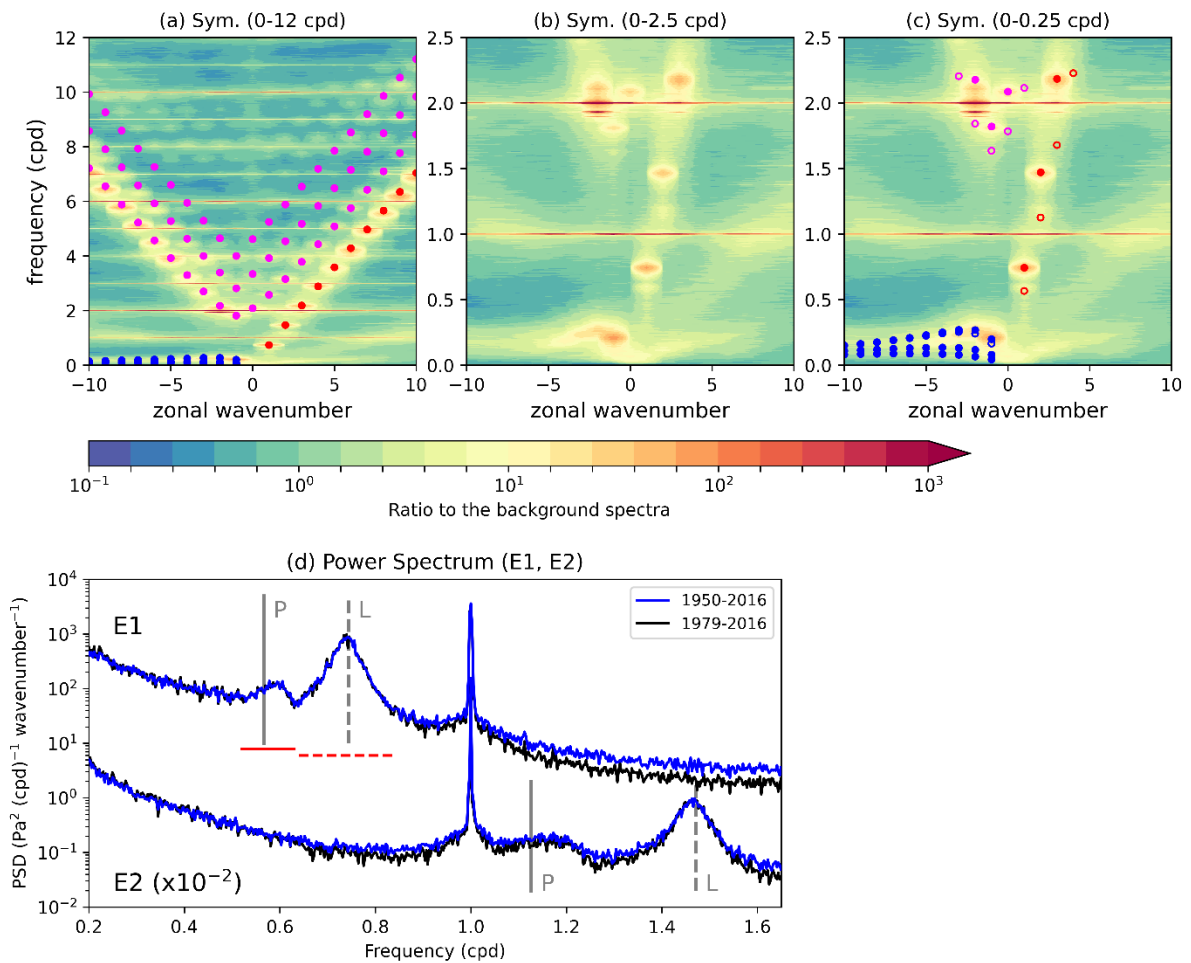


Fig. 9. (a)-(c) Zonal wavenumber-frequency spectrum for equatorially symmetric components calculated with data for 20°S-20°N during 1950-2016. The ratio of the original spectra to the background spectra are shown. (a) is for the frequency range of (a) 0–12 cpd, while (b)-(c) are for that of 0–2.5 cpd. Positive and negative zonal wavenumbers denote eastward and westward phase velocity waves, respectively. For (a) and (c), the theoretical dispersion curves are for $h=10.1$ km (closed circles) and $h=6.1$ km (open circles; only for panel (c)) are overlaid. Blue, red, and magenta circles represent Rossby, Kelvin and gravity modes (for Rossby and gravity, the first three gravest modes are shown). (d) Power spectrum for eastward-propagating wavenumber 1 and 2 components. The latter is multiplied by 10^{-2}

for clarity of presentation. Blue and black curves are the results with data from 1950-2016 and those from 1979-2016, respectively. Gray solid (denoted by "P") and dashed lines (denoted by "L") are for resonant frequencies for $h=6.1$ km and $h=10.1$ km, respectively, for each zonal wavenumber. Horizontal red bars shown for wavenumber 1 are the frequency ranges (0.52-0.63 cpd and 0.64-0.84 cpd) that were used for the filtering that produced the index time series for the two modes.

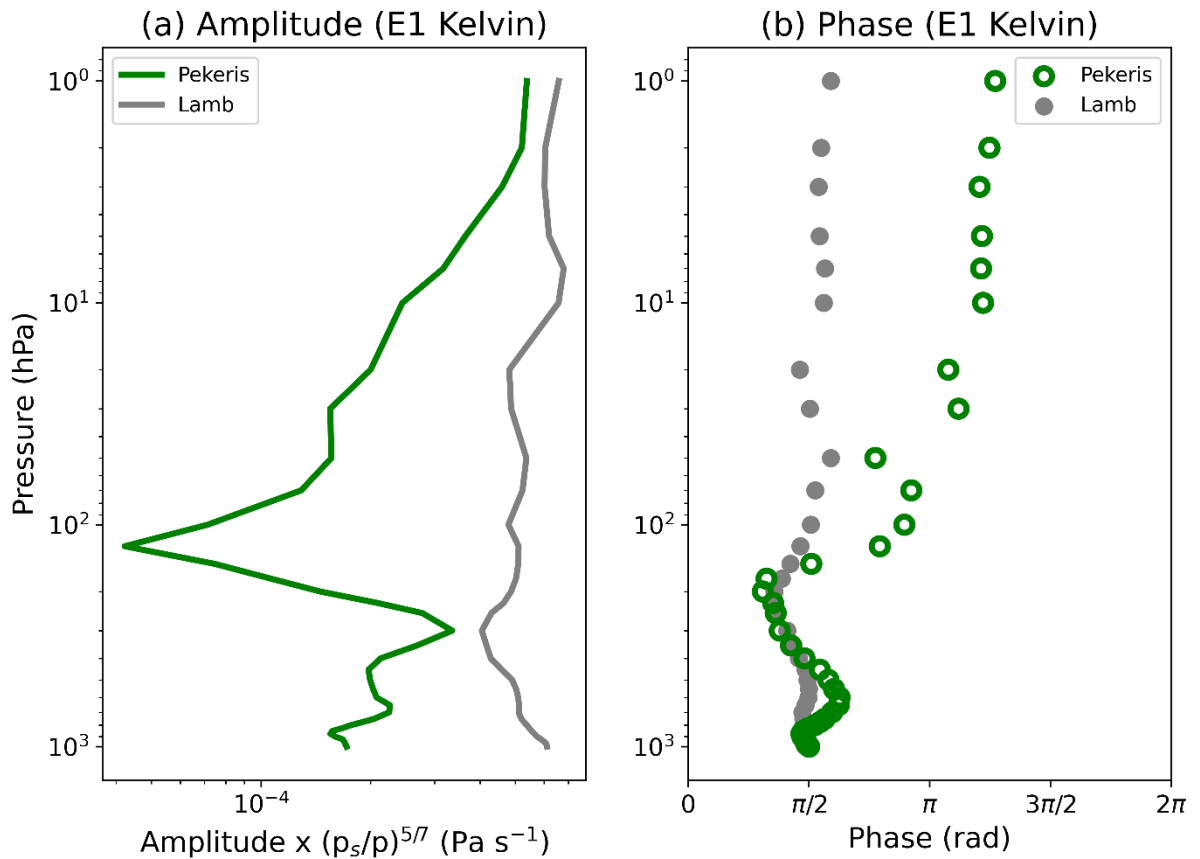


Fig. 10. Vertical profile (up to 1 hPa) of (a) amplitude [Pa s^{-1}] and (b) phase [rad] of equatorially (20°S - 20°N) averaged $\omega \times (P_s/p)^{5/7}$ for the wavenumber 1 Kelvin wave for Lamb (green) and Pekeris modes (gray) as derived by regression onto filtered surface pressure time series over 2010-2016. The amplitude is the regression coefficient multiplied by a factor of $\sqrt{2}\sigma$, where σ is the standard deviation of the index time series. The phase is relative to the variation of surface pressure at 0°E ; the values between 0 and π (π and 2π) denote ω takes a maximum eastward (westward) of pressure maxima.

5. Further Discussion and Conclusions

Nearly a century ago Taylor (1929) showed that the observations following the Krakatoa eruption had implications for understanding the resonant normal modes possible in the atmosphere. In 2022 the Tonga eruption provided a new “natural experiment”, but now in an era with continuous geostationary satellite surveillance and powerful computer simulation capability for the atmosphere. There are likely more lessons to be learned from observations of the full range of atmospheric effects of the eruption, but in this paper we present our initial analysis that demonstrates that the atmosphere can resonate with an internal vertical structure as well as with the familiar external Lamb wave structure.

Specifically we analyzed radiance observations at 10 minute intervals taken from the Himawari 8 geostationary satellite and showed that both a Lamb wave front with the expected horizontal phase speed $\sim 315 \text{ m-s}^{-1}$ and a distinct front with phase speed $\sim 245 \text{ m-s}^{-1}$ can be detected. The slower phase speed is consistent with that expected for the internal Pekeris resonant mode that had been identified in earlier idealized theoretical studies over the past century. We found that the Lamb wave pulse is easily detected in barograph data, as many other observers have noted (Adams, 2022). By using the remarkably dense SORATENA barograph array over Japan, we were also able to convincingly identify the pressure rise and pressure fall of the Pekeris mode wave front as it passed over Japan.

We then performed a global simulation of the eruption aftermath with a high resolution AGCM. The effects of the eruption were introduced by instantaneously adding a hot anomaly over the volcano location. This produced a far field response led by a wave pulse front that had horizontal speed and vertical structure consistent with the Lamb wave. The model results also showed the presence of the slower pulse and that this disturbance had a vertical structure with a 180° phase shift in the lower stratosphere, in agreement with the theoretical prediction for the Pekeris mode.

These observed and model simulation data show that the Pekeris mode can actually be excited and propagate over long distances. We believe that this result conclusively settles the long standing question of the existence (and practical realizability) of an internal Pekeris

682 wave resonance of the atmosphere. It is interesting that Pekeris (1939) realized that if his
683 proposed internal free mode solution existed, then it would open the possibility of an
684 identifiable slower pulse in the 1883 Krakatoa observations. He had only barograph traces at
685 a handful of stations that he could analyze and he found very tentative evidence for a
686 wavefront travelling at a speed corresponding to his suggested $h \sim 8$ km, i.e. just about 10%
687 slower than the Lamb wave. In light of our present results - from satellite and barograph
688 observations following the Tonga eruption and from our computer simulations - we can see
689 that this analysis by Pekeris (1939) is not persuasive, and that the Pekeris mode actually has a
690 significantly slower phase speed corresponding to $h \sim 6$ km (in agreement with the later
691 theoretical predictions by Salby, 1979, 1980).

692
693 Again following Taylor's reasoning, our result for the free waves generated by the
694 volcanic impulse has implications for the spectrum of continuously ringing global mode
695 oscillations in the atmospheric circulation. The two phenomena are closely related, just as
696 the concentric ripples from a stone dropped in a shallow pond and the continuous seiches of
697 the pond are also both manifestations of the same basic dynamics. Once we found that the
698 slower Pekeris mode could be identified in the observed response to the Tonga eruption, we
699 revisited the SH2020 study of the space-time spectrum in the ERA5 data to look for evidence
700 of peaks identifiable as global Pekeris mode oscillations. We found clear evidence for the
701 Pekeris wavenumber 1 and 2 Kelvin modes at frequencies $\sim 20\%$ lower than the
702 corresponding "33 hour" and 16.5 hour" Lamb Kelvin waves.

703
704 The typical surface pressure amplitude of, e.g., the 33 hour Kelvin global normal mode is
705 ~ 0.1 - 0.2 hPa (Hamilton, 1984; SH2020) and the far field pressure perturbations in the main
706 wave front after the Tonga eruption were ~ 2 hPa. Despite the rather modest amplitudes for
707 the phenomena studied here, the improved understanding of the resonant responses of the
708 atmosphere we have achieved may have some practical application to forecasting volcanic
709 eruption hazards and for the important issue of global atmospheric model validation, as
710 explained below.

The ocean response to the underwater eruption of the Hunga Tonga–Hunga Ha'apai volcano surprised scientists as fairly large tsunami waves were observed as far away as Japan and even in the Atlantic (Duncombe, 2022; Robertson, 2022), when the standard view is that underwater volcanic eruptions do not produce large basin-wide tsunamis. This led to speculation that the pressure pulses in the atmosphere may have excited the underlying ocean tsunami response, despite the phase speed of deep water ocean waves being in most places slower than the Lamb wave for a 10 km equivalent depth atmosphere. The possible role of the slower atmospheric Pekeris mode in exciting ocean waves needs to be investigated, possibly with simulations using global ocean models forced with the surface pressure pulses obtained in this study (Suzuki et al., in preparation).

SH2020 suggested that the continuously ringing modes might be considered as quasi-linear systems weakly coupled to the other dynamics in the atmosphere. All the other dynamics then might act as a broad spectral forcing of the normal mode oscillations, leading to Lorentzian spectral response peaks near each of the resonant frequencies; then the width of the spectral response peaks would depend on the global dissipation rate for the modal oscillation. Such a globally-integrated dissipation rate is hard to otherwise diagnose empirically, so the global mode spectra hold potentially important information for understanding the general circulation. Of course, if the nonlinearity affecting the modes is sufficiently strong, then the interpretation may not be so simple (Zurita-Gotor and Held, 2021; hereinafter ZH). In any event, the spectral widths in models can be expected to depend on the assumed physical parameterizations and so the observations can provide a valuable avenue for model validation. ZH showed that a simplified AGCM reproduced many of the Lamb wave normal mode peaks identified earlier in observations by SH2020, but the peaks were somewhat narrower in their model simulation than in the SH2020 results. ZH suggested that the difference might be a result of the simplifications in their model (e.g., no topography, simplified moist physics).

Now, with the discovery of the Pekeris mode in the long record of observations, we have another target for global model validation. Our Figure 9d demonstrates that, at least for the wavenumber 1 and 2 Kelvin modes, the available ERA5 observational record appears

sufficiently long to accurately delineate the detailed spectral shape of the peaks associated with the Pekeris mode.

The present paper has made the case for the realizability of global resonant modes with the internal Pekeris vertical mode structure, but much more work remains to be done on the Lamb and Pekeris modes both in their role in the response to the Tonga eruption and as continuously ringing modes in the atmosphere. As noted above, the comparison of the observed spectrum of continuously ringing modes with those in long simulations using comprehensive global models is potentially very interesting, and such comparisons have just barely begun so far.

Finally we note again that our analysis of the atmospheric perturbations caused by the recent Tonga eruption is preliminary in that we have analyzed only limited data (geostationary satellite radiance data and surface pressure from just Hawaii and from Japan) and conducted just one model simulation for only the first 12 hours after the eruption. There is more to be learned by expanding the scope of the investigations beyond these limits. When an explosive impulse occurs, the initial perturbation will project onto a range of free atmospheric waves including both vertically propagating waves and purely horizontally propagating Lamb and Pekeris modes. The vertically propagating waves can be expected to be dissipated high in the atmosphere, while the far field response in the lower atmosphere will be dominated by wave front pulses associated with the Lamb and Pekeris modes. In the simplest view the pulses will each propagate non-dispersively at the speed \sqrt{gh} . Actually the component of the initial perturbation projecting onto, say, the Lamb wave in the vertical will itself project onto a complicated set of horizontal modes with different phase speeds. Thus we should anticipate some dispersion of the normal mode pulses as they propagate away from the eruption. In the limit of a very short pulse, though, we expect the projection to be dominated by high wavenumber and frequency components whose phase seeds asymptote to \sqrt{gh} (see Fig. 9a). For a finite length initial pulse there will be some degree of dispersion and this may be observable and again an aspect that could help validate global model simulation.

In the high-frequency limit and for the idealized situation of a motionless mean state the pulses from an isolated initial perturbation will expand outward in concentric circles. However, Taylor (1929) noted that the Krakatoa wave front was observed to depart from circularity and developed a roughly wave-3 deformation, which he showed likely came principally from Doppler shifting by the mean winds. In our simulation we found evidence of anisotropy in the far field wave fronts from the Tonga eruption. It appears that the deviation from idealized behavior of the wave fronts is greater for the Pekeris mode than for the Kelvin mode. This makes sense given the lower phase speed of the Pekeris mode and the fact that the Pekeris mode activity is more weighted to the stratosphere and mesosphere where mean winds may be strong.

We applied the remarkably dense SORATENA array barograph data in over Japan to detect the wave fronts and even sample the detailed structure of the pressure pulses. In the period after the eruption there are high frequency data from likely hundreds of other locations throughout the world. It remains to combine all these data to characterize in detail the Lamb wave front as it travelled around the globe several times. Specifically it would be desirable to characterize the position of the front and then the shape of the pulse at each location around the front. The evolution of the Lamb pulse would depend on dispersion, dissipation and the effects of the non-constant mean background and even possibly on "scattering" of the wave by topography. Once the data are summarized in a systematic fashion the result could be compared with high resolution global model simulations extended out to several days after the eruption.

Acknowledgments.

This study was supported by the Integrated Research Program for Advancing Climate Models (TOUGOU) Grant Number JPMXD0717935715 from the Ministry of Education, Culture, Sports, Science and Technology (MEXT), Japan. T.S. and M.N. were supported in part by the MEXT through Grants-in-Aid for Scientific Research (21K03661 and JP20H05728). The simulations in this study were performed using the Earth Simulator at the Japan Agency for Marine-Earth Science and Technology (JAMSTEC). Himawari 8 gridded

data are distributed by the Center for Environmental Remote Sensing (CEReS), Chiba University, Japan. The barographic pressure data of the SORATENA array were provided by Weathernews Inc. The GFD-DENNOU Library, GTOOL, and Panoply (<https://www.giss.nasa.gov/tools/panoply/>) were used to draw figures.

Data Availability Statement.

All the simulation data necessary for re-producing figures in this study are available at <https://doi.org/10.5281/zenodo.6394322>. The Himawari 8 gridded data are available at <ftp://hmwr829gr.cr.chiba-u.ac.jp/gridded/FD/V20190123/>. The MERRA-2 data are available at https://disc.gsfc.nasa.gov/datasets/M2I3NVASM_5.12.4/summary. The barographic pressure data in Japan is available upon request at <https://global.weathernews.com/news/16551/>. The barographic pressure data off Honolulu is available at https://www.ndbc.noaa.gov/station_realtime.php?station=oouh1. The ERA5 reanalysis data are available at <https://cds.climate.copernicus.eu/cdsapp#!/dataset/reanalysis-era5-single-levels?tab=overview> for the mean sea-level pressure and <https://cds.climate.copernicus.eu/cdsapp#!/dataset/10.24381/cds.bd0915c6?tab=overview> for the geopotential height, respectively.

APPENDIX A

Chaim Pekeris and the “Pekeris mode”

The American-Israeli physicist and applied mathematician Chaim Pekeris (1908-1993) was a remarkable scientist whose work spanned meteorology, oceanography, solid earth geophysics, astrophysics and even atomic physics. According to his US National Academy of Science biography (Gilbert, 2004) Pekeris was regarded as “the founding father” of the Faculty of Mathematics and Computer Science of Israel’s Weizmann Institute of Science, while other sources have called him “the father of Israeli geophysics”. Pekeris’ work on the normal mode solutions for the atmosphere (Pekeris, 1937, 1939) was an early contribution following his 1933 doctorate in meteorology from MIT (Gilbert, 2004). We feel that - now that we have verified Pekeris’ basic idea - his very original contribution should be acknowledged by adopting the term “Pekeris mode”. This makes a nice symmetry with the term “Lamb mode” which acknowledges the key contribution of the English physicist Horace

Lamb (1849-1934). It turns out that the young Pekeris was very much influenced by Lamb's work on wave motion, and Gilbert (2004) claims that Pekeris had "practically memorized" one Lamb paper and had even borrowed the relevant the journal volume from the MIT library for several months by constantly renewing every two weeks (this was before xerox machines!). It is fitting that our proposed nomenclature will link Chaim Pekeris' name with that of his personal scientific hero and inspiration, Horace Lamb.

REFERENCES

- Adam, D., 2022: Tonga volcano created puzzling atmospheric ripples. *Nature*, **602**, 497, doi: <https://doi.org/10.1038/d41586-022-00127-1>.
- Bowditch, N., 1829: *Mécanique Céleste* of the Marquis de La Place translated with a commentary by Nathaniel Bowditch. Hilliard, Gray, Little, and Wilkins Publishers, Boston.
- Chapman, S., 1924: The semidiurnal oscillation of the atmosphere. *Quart. J. Roy. Meteorol. Soc.*, **50**, 165–193, <https://doi.org/10.1002/qj.49705021102>.
- Chapman, S., and R. Lindzen, 1970: *Atmospheric tides: Thermal and gravitational*. D. Reidel, New York, 200 pp.
- Duncombe, J., 2022: The surprising reach of Tonga's giant atmospheric waves. *Eos*, **103**, <https://doi.org/10.1029/2022EO220050>.
- Forbes, J. M., and X. Zhang, 2012: Lunar tide amplification during the January 2009 stratosphere warming event: Observations and theory. *J. Geophys. Res.*, **117**, A12312, <https://doi.org/10.1029/2012JA017963>.
- Gilbert, F., 2004: Chaim Leib Pekeris 1908-1993. *Biographical Memoirs of the National Academy of Sciences*, **85**, 1-17.
- Global Modeling and Assimilation Office (GMAO) (2015), MERRA-2 inst3_3d_asm_Nv: 3d,3-Hourly,Instantaneous,Model-Level,Assimilation,Assimilated Meteorological Fields V5.12.4, Greenbelt, MD, USA, Goddard Earth Sciences Data and Information Services Center (GES DISC), Accessed: [27 February 2022], 10.5067/WWQSXQ8IVFW8

865 Hamilton, K., 1984: Evidence for a normal mode Kelvin wave in the atmosphere. *J.*
866 *Meteorol. Soc. Japan*, **62**, 308–311, https://doi.org/10.2151/jmsj1965.62.2_308.

867 Hamilton, K., 2020: The discovery of the stratopause and mesosphere. *SPARC Newsletter*,
868 **55**, 26–30, available at <http://www.sparc-climate.org/publications/newsletter>.

869 Hamilton, K., and R. R. Garcia, 1986: Theory and observations of the short-period normal
870 mode oscillations of the atmosphere. *J. Geophys. Res.*, **91** (D11), 11,867–11,875,
871 <https://doi.org/10.1029/JD091iD11p11867>.

872 Hirota, I., and T. Hirooka, 1984: Normal mode Rossby waves observed in the upper
873 stratosphere. Part I: First symmetric modes of zonal wavenumbers 1 and 2. *J. Atmos. Sci.*,
874 **41** (8), 1253–1267, [https://doi.org/10.1175/1520-](https://doi.org/10.1175/1520-0469(1984)041<1253:NMRWOI>2.0.CO;2)
875 [0469\(1984\)041<1253:NMRWOI>2.0.CO;2](https://doi.org/10.1175/1520-0469(1984)041<1253:NMRWOI>2.0.CO;2).

876 Hough, S.S., 1897: On the application of harmonic analysis to the dynamical theory of tides.
877 Part I: On Laplace’s ‘Oscillations of the first species’, and on the dynamics of ocean
878 currents. *Phil. Trans. Roy. Soc.*, **A189**, 201–257, <https://doi.org/10.1098/rsta.1897.0009>.

879 Hough, S.S., 1898: The application of harmonic analysis to the dynamical theory of tides.
880 Part II: On the general integration of Laplace’s dynamical equations. *Phil. Trans. Roy.*
881 *Soc.*, **A191**, 139–185, <https://doi.org/10.1098/rsta.1898.0005>.

882 Jacchia, L.G., and Z. Kopal, 1952: Atmospheric oscillations and the temperature profile of
883 the upper atmosphere. *J. Meteor.*, **9**, 13–23, [https://doi.org/10.1175/1520-](https://doi.org/10.1175/1520-0469(1952)009<0013:AOATTP>2.0.CO;2)
884 [0469\(1952\)009<0013:AOATTP>2.0.CO;2](https://doi.org/10.1175/1520-0469(1952)009<0013:AOATTP>2.0.CO;2).

885 Lindzen, R.S., E.S. Batten, and J.-W. Kim, 1968: Oscillations in atmospheres with tops. *Mon.*
886 *Wea. Rev.*, **96**, 133–140, doi:10.1175/1520-0493(1968)096<0133:OIAWT>2.0.CO;2.

887 Matsuno, T., 1980: A trial of search for minor components of lunar tides and short period
888 oscillations of the atmosphere in surface pressure data. *J. Meteorol. Soc. Japan*, **58**, 281–
889 285, https://doi.org/10.2151/jmsj1965.58.4_281.

890 Pekeris, C.L., 1937: Atmospheric oscillations. *Proc. Roy. Soc.* **A158**, 650–671.

891 Pekeris, C.L., 1939: Propagation of a pulse in the atmosphere. *Proc. Roy. Soc.* **A171**, 434–
892 449.

Robertson, R.G., 2022: Tonga shock wave created tsunamis in two different oceans. *AAAS Science*, <https://www.science.org/content/article/tonga-shock-wave-created-tsunamis-two-different-oceans>

Sakazaki, T., and K. Hamilton, 2020: An array of ringing global free modes discovered in tropical surface pressure data. *J. Atmos. Sci.*, **77**, 2519–2539, <https://doi.org/10.1175/JAS-D-20-0053.1>.

Salby, M., 1979: On the solution to the homogeneous vertical structure problem. *J. Atmos. Sci.*, **36**, 3250–3259, [https://doi.org/10.1175/1520-0469\(1979\)036<2350:OTSOTH>2.0.CO;2](https://doi.org/10.1175/1520-0469(1979)036<2350:OTSOTH>2.0.CO;2).

Salby, M., 1980: The influence of realistic dissipation on planetary normal structures. *J. Atmos. Sci.*, **37**, 2186–2199, [https://doi.org/10.1175/1520-0469\(1980\)037<2186:TIORDO>2.0.CO;2](https://doi.org/10.1175/1520-0469(1980)037<2186:TIORDO>2.0.CO;2).

Strachey, R., 1888: On the air waves and sounds caused by the eruption of Krakatoa in August 1883. In G.J. Symons (Ed.), *The Eruption of Krakatoa, and Subsequent Phenomena*, Trübner & Co., London. pp. 57–88.

Takenaka, H., T. Sakashita, A. Higuchi, and T. Nakajima, 2020: Development of geolocation correction for geostationary satellite observation by phase only correlation method using visible channel. *Remote Sensing*, **12** (15), 2472, <https://doi.org/10.3390/rs12152472>.

Taylor, G.I., 1929: Waves and tides in the atmosphere. *Proc. Roy. Soc. Lond.*, **A126**, 169–183, <https://doi.org/10.1098/rspa.1929.0213>.

Thomson, W., 1882: On the thermodynamic acceleration of the earth's rotation. *Proc. Roy. Soc. Edinb.*, **11**, 396–405, <https://doi.org/10.1017/S037016460004757X>.

Watanabe, S., and S. Miyahara, 2009: Quantification of the gravity wave forcing of the migrating diurnal tide in a gravity wave–resolving general circulation model. *J. Geophys. Res.*, **114**, D07110, doi:10.1029/2008JD011218.

Whipple, F.J.W., 1934: On phenomena related to the great Siberian meteor. *Quart. J. Roy. Meteorol. Soc.*, **60**, 505–513, <https://doi.org/10.1002/qj.49706025709>.

Yamamoto, R., 1956: The microbarographic oscillations produced by the explosions of hydrogen bombs in the Marshall Islands. *Bull. Amer. Meteorol. Soc.*, **37**, 406–409, <https://doi.org/10.1175/1520-0477-37.8.406>.

- 923 Yamamoto, Y., K. Ichii, A. Higuchi, and H. Takenaka, 2020: Geolocation accuracy
924 assessment of Himawari-8/AHI imagery for application to terrestrial monitoring, *Remote*
925 *Sensing*, **12** (9), 1372, <https://doi.org/10.3390/rs12091372>.
- 926 Zurita-Gotor, P., and I. Held, 2021: Westward-Propagating Rossby Modes in Idealized
927 GCMs. *J. Atmos. Sci.*, **78**, 1503–1522, <https://doi.org/10.1175/JAS-D-20-0276.1>.
- 928